1 Seismic evidence for tectonism-dominant seafloor spreading in the Southwest Sub-basin, South

2 China Sea

3 Junhui Yu [a,b], Pin Yan [a,*], Yanlin Wang [a], Jinchang Zhang [a], Yan Qiu [c], Manuel Pubellier [d]

4 [a] CAS Key Laboratory of Ocean and Marginal Sea Geology, South China Sea Institute of Oceanology,

5 Chinese Academy of Sciences, No.164 West Xin'gang Rd., 510301 Guangzhou, China

6 [b] University of Chinese Academy of Sciences, No.19 Yuquan Rd., 100049 Beijing, China

7 [c] Guangzhou Marine Geological Survey, Ministry of Land and Resources, P.O. BOX 1180, Nan'gang,

8 510760 Guangzhou, China

9 [d] Laboratoire de Géologie, École Normale Supérieure, CNRS/UMR 8538, 24 rue Lhomond, 75005

10 Paris, France

11 **Abstract:** Seafloor spreading can occur in different dynamic mechanisms, magma- or

12 tectonism-dominant. The Southwest Sub-basin located at the southwest tip of the propagating

13 seafloor spreading of the South China Sea, remains unclear for its spreading dynamic owing to poor

14 and debated knowledge of the crustal structures. Here, two long streamer (6 km) multi-channel

15 seismic lines and one coincident seismic refraction line across the Southwest Sub-basin are

16 reprocessed and analyzed with focus on crustal imaging. The sediments are usually 0.5 km to 1 km

17 thick over the abyssal basin, more or less thicker in the few grabens and thickest in the median valley.

18 The basement is fairly rough and highly faulted by ubiquitous crustal faults. Both multi-channel

19 seismic lines show only few visible reflectors at 1.5 to 3.6 km depth below the fragmented basement

20 mostly as intermittent and diffusive reflections. They correlate with the 6.8-7.2 km/s contours

21 obtained from velocity inversion of refraction seismic data, thus reasonably interpreted as the

22 reflection seismic Moho. Therefore, the crustal thickness is only 1.5-3.6 km excluding sediments.

23 Beneath this thin crust is a velocity-gradient zone with velocities gradually increasing to 8.0 km/s

24 downwards, which may result from partial serpentinization of upper mantle rocks facilitated by

25 numerous deep-penetrating faults which accommodate paths for sea water infiltration. Furthermore,

26 the fault-bounded fossil spreading center is a negative median valley and its basement is 3.3 km

27 deeper at most than the surrounding area. These features, remarkably different from the East and

*Corresponding author at: CAS Key Laboratory of Ocean and Marginal Sea Geology, South China Sea Institute of Oceanology, CAS, No. 164 West Xin'gang Rd., Guangzhou 510301, China. Tel.: +86 20 34066182 fax: +86 20 84451672.
Email address: yanpin@scsio.ac.cn

Northwest Sub-basins of the South China Sea where normal oceanic crust and positive or featureless mid-ridges developed, imply that the development of the Southwest Sub-basin was tectonism-dominant or magma-poor and the magma supply decreased with the southwestern propagation of the seafloor spreading from the eastern part of the South China Sea.

Keywords: Southwest Sub-basin of the South China Sea; Reflection seismic Moho; Thin crust; Partially serpentinized mantle; Poor magmatism

1. Introduction

Seafloor spreading involves the closely linked processes of magmatism and tectonic extension, and can be divided into two types: magmatism-dominant (magma-rich) and tectonism-dominant (magma-poor) based on its dominant dynamic process (Mutter and Karson, 1992). The South China Sea (SCS) has experienced initial magma-poor continental rifting and subsequent oceanic seafloor spreading from the Late Cretaceous to Middle Miocene (Taylor and Hayes, 1983; Briais et al, 1993; Yan et al, 2001; Barckhausen and Roeser, 2004; Expedition 349 Scientists, 2014; Franke et al, 2014; Li et al, 2014), generating three oceanic sub-basins: the Northwest Sub-basin (NWSB), the East Sub-basin (ESB) and the Southwest Sub-basin (SWSB) (Fig.1). It is commonly agreed that the seafloor spreading occurred firstly in the ESB and then propagated southwestwards to the SWSB with a re-orientation of the spreading center from E-W to NE-SW. In the ESB and NWSB, the oceanic basement is fairly flat with only minor normal faults except a few seamounts. The crust there is also fairly uniform with an average thickness of 6.0 km, reviewing from the only few published multi-channel seismic (MCS) profiles (McIntosh et al, 2014; Cameselle et al, 2015; Sun et al, 2016). The crustal features in these two sub-basins are comparable to the typical crust created by magma-rich seafloor spreading, e.g. the case of the eastern Ogasawara Plateau and East Pacific Rise (White et al, 1992; Tsuji et al, 2007; Aghaei et al, 2014). However, as the southwest tip of the propagating seafloor spreading of the SCS, the SWSB remains unclear for its spreading dynamic owing to poor and debated knowledge of the crustal structures.

Several geophysical surveys have been conducted to study the crustal structure of the SWSB (Braitenberg et al, 2006; Qiu et al, 2011; Pichot et al, 2014; Yu et al, 2016; Zhang et al, 2016). The crustal thickness inverted from satellite derived gravity data (Braitenberg et al, 2006) is only 1-4 km excluding sediments, which is too thin to be a normal oceanic crust (White et al, 1992), indicating that the seafloor spreading in the SWSB was magma-poor. Only three oceanic bottom seismometer

(OBS) surveys (OBS973-1 and OBS973-3 (Qiu et al, 2011; Yu et al, 2016), CFCST-OBS2011 (Pichot et al, 2014), T1 (Zhang et al, 2016); Fig.2) have been carried out in the SWSB. In line CFCST-OBS2011, only three OBSs were deployed in the basin area with an average spacing of ~80 km, and line T1 simply focused on the fossil spreading center in the northeastern SWSB. So line OBS973-1 and OBS973-3 with 11 OBSs in the basin area are the most favorable refraction data left for studying the crustal structure of the SWSB. The results of line OBS973-1 and OBS973-3 published before (Qiu et al, 2011; Yu et al, 2016) suggested that the crust of the SWSB is normal Atlantic-type oceanic crust with crustal thickness of 5-6 km and a sharp velocity jump from 6.9-7.2 km/s to 8.0 km/s exists in the crust-mantle boundary. However, these results were obtained from forward modeling (Zelt and Smith, 1992), which strongly requires a priori information, inevitably involves some degree of subjectivity and potentially results in velocity jumps at layer boundaries (Delescluse et al, 2015; Davy et al, 2016). The almost absence of PmP (Moho reflections) arrivals in the basin area of line OBS973-1, OBS973-3 and CFCST-OBS2011 (Qiu et al, 2011; Pichot et al, 2014; Yu et al, 2016) also indicates that there might be a gradual transition zone between the crust and mantle rather than a sharp boundary. Therefore, it is necessary to reprocess the data of OBS973-1 and OBS973-3 with the travel-time tomography inversion (Zelt and Barton, 1998; Korenaga et al, 2000; Hobro et al, 2003) which does not require any other priori information apart from a loose initial velocity model, to lower the risk of pre-inversion over-interpretation and generate more objective velocity model.

In addition, the reflection Moho has been barely imaged from previous MCS profiles (Zhao et al, 2011; Li et al, 2012; Song and Li, 2015; Ding et al, 2016), leading to the undefined reflection crustal structure of the SWSB. In this study, we first reprocess two MCS lines (NH973-1 and CFCST-MCS2013, Fig.2) focusing on the imaging of deep reflections and one OBS line (OBS973: the basin area of OBS973-1 and OBS973-3, Fig.2) with the code of First Arrival Seismic Tomography (Zelt and Barton, 1998). Then we present and finally discuss the results in terms of crustal structure, with a particular focus on the dynamic origin during the formation of the SWSB.

2. Geological setting

The SCS is a relatively young marginal sea offshore East and Southeast Asia. Prior to the continental rifting and subsequent seafloor spreading of the SCS, East Asia experienced the

subduction of paleo-Pacific plate through most of the Paleozoic and Mesozoic. The initial rifting of the SCS started at ~65 Ma when the convergent margin changed to extension. In the mid-Cenozoic, after the breakup of the lithosphere in the South China continent, seafloor spreading began firstly from the ESB at about 33-31 Ma, then propagated to the SWSB at about 27-23.6 Ma accompanying the southward ridge jump in the ESB, and ended almost synchronously in both sub-basins at ~15.5 Ma (Taylor and Hayes, 1983; Briais et al, 1993; Barckhausen and Roeser, 2004; Expedition 349 Scientists, 2014; Li et al, 2014). Constrained by magnetic anomalies and IODP Expedition 349 drilling results, Li et al. (2014) estimated that the ESB spread at slow to intermediate (full spreading rate: ~20 to ~80 mm/yr) rate and the SWSB at slow (~50 to 35 mm/yr) rate. However, the opening mechanism of the SCS remains controversial. The extrusion model proposed by Tapponnier et al. (1982, 1986) suggests that the rotation and extrusion of the Indochina Peninsula account for the opening of the SCS. Another widely discussed mechanism attributes the opening to the slab pull from the subduction of a proto-South China Sea to the south (Taylor and Hayes, 1983; Hall, 2002, 2009; Pubellier et al, 2004).

The SCS basin is a rhomb-shaped oceanic basin developed by approximately N-S to NW-SE oriented seafloor spreading with a pair of conjugate continental margins, the South China continental margin in north and the Nansha islands block in south (Fig.1). These margins are rich in highly faulted and extended continental blocks (Huang et al, 2005; Ding et al, 2013; Franke et al, 2014; Sun et al, 2016) with large rifted basins, such as Pearl River Mouth and Southwest Taiwan Basins in the north margin and Liyue and Zhenghe Basins in the south margin. Additionally, owing to the fact that very weak syn-rift magmatism and volcanism have been recognized, they are deemed as non-volcanic margins (Yan et al, 2001; Yan et al, 2006; Franke et al, 2014). In addition, the northern margin of the SCS features significant longitudinal morphologic variations. While the eastern part of the northern margin shows 400 km of extended crust, the continental crust extends to nearly 800 km in the western part (Fig.1), suggesting that different modes of extension prevailed along the continental margins of the SCS (Hayes and Nissen, 2005 ; Pichot et al, 2014).

Located in the southwest of the SCS, the SWSB is a V-shaped sub-basin opening to the northeast, and its water depth is mostly at ~4300 m which is deeper than the average water depth in both ESB and NWSB (Fig.1). Its northwest continental margin is occupied by Zhongsha-Xisha islands block, and its southeast margin is sit with Nansha islands block. To the east, the SWSB is separated from

the ESB by Zhongnan fracture zone (Fig.1). Similar to margins of the ESB, its northwest margin also exhibits non-volcanic features, such as highly faulted and thinned continental crust, a number of rifted basins (e.g. Zhongjiannan Basin and Qiongdongnan Basin) developed with unobvious magma underplating, and only sporadic volcanism during rifting and spreading (Lü et al, 2011; Qiu et al, 2011; Savva et al, 2013; Pichot et al, 2014). Post-rift tectonic extension significantly weakens but persists in both the margins evidenced by young normal faults (Ding et al, 2013; Savva et al, 2013). On the bathymetric map, the SWSB features a northeast-oriented and spatially varying fossil spreading center, which comprises three different segments: (S1) several large seamounts in the northeast, (S2) a ~100 m deep depression bounded by two remarkable linear rift shoulders in the center and (S3) flat seafloor in the southwest (Fig.1). There are several seamounts scattered in the northeastern segment (S1) of the fossil spreading center which are dated as post-spreading (Fig.1) (Wang et al, 1985; Yan et al, 2008; Yan et al, 2014). For example, the ages of samples D10 and S04-14-1 dredged from the Zhongnan seamount (Fig.1) are ~6.6-3.5 Ma measured by K-Ar dating of alkaline basalts. However, in the depression of the central segment (S2), the Longmen Seamount, ~1400 m high and ~20 km wide, has been identified as an anomalous seamount composed of low-density materials rather than igneous rocks (Wang et al, 2017).

3. Data acquisition and processing

3.1 MCS and OBS data acquisition

MCS lines NH973-1 and CFCST-MCS2013 cross the central segment (S2) of the SWSB in NNW-SSE and NW-SE direction, respectively (Fig.2). Line NH973-1 was acquired with the *R/V* Tanbao of Guangzhou Marine Geological Survey in 2009, and Line CFCST-MCS2013 was obtained with the *R/V* Dong Fang Kan Tan No.1 along OBS profile CFCST-OBS2011 in 2013. The acquisition parameters are listed in Table.1. Both MCS lines were conducted with a long streamer of 6 km and shot by an air-gun array with a large volume of 83.3 L (5080 cu in), providing us with great possibility of imaging the deep crustal structures.

In this study, we also present one OBS line (OBS973) collected along MCS line NH973-1 (Fig.2). In 2009 and 2011, two OBS lines (OBS973-1 and OBS973-3) were acquired onboard R/V Shiyan2 of South China Sea Institute of Oceanology, Chinese Academy of Sciences. Line OBS973-1 cross the SWSB and southern continental margin, and line OBS973-3 is located to the north of

148 OBS973-1 and across the northern margin. A total of 20 OBSs were deployed along each line with

149 the instrument spacing of approximately 20 km. The air gun array was composed of 4×24.5 L BOLT

150 guns with a total volume of 98 L (6000 cu in). Shots were time triggered every 60-120 s,

151 corresponding to ~150-300 m distance at a cruise speed of 5 knots. Finally, 19 OBSs of OBS973-1

152 were recovered but one OBS recorded no data, and 19 OBSs were successfully recovered along

153 OBS973-3. As the basin area was our focus, here 15 OBSs (OBS21-22, 24-29, 31-33 from line

154 OBS973-1 and OBS01-02, 04-05 from line OBS973-3) located near the COT and in the basin area

155 were involved to form the line OBS973 (Fig.2).

156 3.2 MCS data processing

157   MCS line NH973-1 has been processed by China National Offshore Oil Corporation (CNOOC)

158 (Liu and Yu, 2009) and published focusing on the shallow crustal structure (Zhao et al, 2011; Li et al,

159 2012; Ding et al, 2016). However, the deep reflections, especially Moho, can hardly be seen,

160 probably because the attenuation of peg-leg multiples was seriously neglected (Liu and Yu, 2009).

161 The seafloor, basement and some sediment interfaces are strong wave impedance interfaces in the

162 oceanic basin area, resulting in notorious peg-leg multiples which seriously mask the deep reflections

163 (Fig.3a). Therefore, we reprocessed this data with great concentration on the suppression of peg-leg

164 multiples to clearly image the deep crustal structure and Moho.

165   Among both MCS lines, our data processing included resampling to 4 ms, trace edit, static

166 correction, noise attenuation, spherical divergence correction, CDP sorting, velocity analysis, peg-leg

167 multiples attenuation, NMO, stack, finite-difference time migration, and band-pass filtering. The

168 attenuation of peg-leg multiples consisted of two procedures: parabolic Radon transform filtering and

169 inner muting. According to the velocity difference between the peg-leg multiples and the signals,

170 parabolic Radon transform filtering was firstly applied to suppress the multiples in the middle and far

171 offset (Fig.3b). Then, the inner muting was carried to further remove the residual multiples in the

172 near traces (Fig.3c). The peg-leg multiples have been effectively attenuated and the deep reflection

173 signals have been greatly imaged (Fig.3, Yu et al, 2017). In addition to these processing steps, both

174 MCS profiles were converted to depth using the smoothed interval velocities constrained by velocity

175 analyses and the tomographic velocity models inverted from OBS data (Fig.10d and Pichot et al,

176 2014).

177 3.3 OBS data processing

The data of line OBS973 has been published by Qiu et al. (2009) and Yu et al. (2016). Their velocity models obtained from forward ray tracing (Zelt and Smith, 1992) show that the crust nature of the SWSB is normal Atlantic-type oceanic crust with crustal thickness of 5-6 km, and there is a sharp velocity jump from ~6.9-7.2 km/s to 8.0 km/s in the crust-mantle boundary. However, forward ray tracing inevitably involves some degree of subjectivity and potentially leads to overinterpretation because the layer geometry and velocity gradients are chosen manually (Delescluse et al, 2015). Among the 11 OBSs of line OBS973 in the basin area, the PmP phases can be poorly identified (Fig.4) and only two OBSs (OBS 27 and 29) show short-range, unclear PmP phases with high uncertainty (Qiu et al, 2011; Yu et al, 2016). The rare PmP reflections are insufficient to constrain the geometry of the crust-mantle boundary and also imply transition zone instead of velocity jump between the crust and mantle.

In contrast, the more commonly-used method to develop P wave velocity models based on OBS data are traveltime tomography inversions (Zelt and Barton, 1998; Korenaga et al, 2000; Hobro et al, 2003), which achieves much greater objectivity. Generally, the velocity models inverted by traveltime tomography are slightly dependent on the starting model, enabling us to avoid making more assumptions on the unknown part and lower the risk for pre-inversion over-interpretation. So we reprocessed the line OBS973 using Fast Tomography code (Zelt and Barton, 1998) which is a popular approach of first-arrival traveltime tomography inversion.

Before first-arrival picking and traveltime tomography, several preprocessing steps should be done, including clock correction, relocation of OBSs, and band-pass filtering (5-15 Hz). Shot delay and linear clock-drift corrections were carried to synchronize the OBS clock with GPS time. The relocation of OBSs was performed using the water wave traveltimes to correct their drifts during the descent to the seafloor. Then, we picked all the first arrivals with an uncertainty of 20-60 ms depending on the signal-to-noise ratio. Generally, the uncertainty of 20 ms is for the water wave and near-offset (<30 km) arrivals and an average uncertainty of 40 ms corresponds to the offset between 30 km and 70 km, while the large offset (>70 km) picks get a picking uncertainty of 60 ms. The model size of line OBS973 is 370 km×25 km. The starting model was divided into 1481×101 grids with each grid size of 0.25 km×0.25 km. In the initial velocity model, the geometry of seafloor is constrained by the reflection seismic profiles NH973-1 and NH973-1a (Zhao et al, 2011) and the water layer upon the seafloor gets a constant velocity of 1.5 km/s. The velocity linearly increases

from 1.5 km/s at the seafloor to 8.0 km/s at a depth that is 10 km in the basin area and gradually increases to 18 km in the model edges (Fig.10a). We then consider that velocities slowly increase downward. The result of the first-arrival tomography inversion based on this initial model will be presented in section 4.2.

4. Results

4.1 MCS profiles

Fig.5a and Fig.5b are the depth-converted MCS profiles NH973-1 and CFCST-MCS2013, respectively. The enlarged and interpreted sections of profiles NH973-1 and CFCST-MCS2013 are shown in Figures 6, 7, 8 and 9. The locations of magnetic isochrones obtained from Briais et al, 1993 are also shown in these figures.

The seafloor of the SWSB is fairly flat, contrasting with a rough basement (Fig.5-9). The sedimentary sections are clearly visible above basement and usually 0.5 km to 1 km thick over the abyssal basin, more or less thicker in some local deep sedimentary basins. The sediments are thickest (3.3 km) in the fossil spreading center and relatively thin in both sides of NH973-1 (Fig.5a). However, they are extremely thin (0-0.3 km) in the fossil spreading center of CFCST-MCS2013 (Fig.5b), because the spreading center in this small section has been occupied by an isolated seamount (Longmen Seamount) with an anomalously low density (2.33 g/cm^3; Wang et al, 2017) (Fig.2). The sedimentary sequences are mostly sub-horizontal, finely layered and lack of syn-tectonic wedges in both profiles. Locally, the reflectors within sediments exhibit young normal faulting (e.g. at 75 km in NH973-1 and 160-180 km in CFCST-MCS2013). In addition, there are some sub-horizontal strong reflectors within shallow sedimentary layers (e.g. at 95-135 km in NH973-1 and 70-90 km in CFCST-MCS2013), which probably are sills (Fig.6~Fig.8).

The basement in most places can be easily identified from its strong reflectivity beneath the more transparent and stratified sediments, excluding local areas (e.g. at 110-140 km in NH973-1 and 75-90 km in CFCST-MCS2013) where sills always exist above (Fig.6~Fig.8). The basement is greatly undulating owing to the basement highs (indicated by H1-H4 in NH973-1 and H1-H9 in CFCST-MCS2013) and rift shoulders (Fig.5~Fig.9). On top of some basement highs (H1 and H3 in NH973-1 and H1-H2 in CFCST-MCS2013) and rift shoulders, the layered sediments are locally tilted and lie subparallel to the adjacent basement surface. Numerous deep normal faults cut the

basement into many different sections, leading to the formation of the basement highs and seamounts accompanying with magmatic intrusion and eruption (Fig.6~Fig.9). These deep faults which control the faulted blocks mainly dip away from the spreading axis, but there are still many faults symmetrically distributed around some local deep sedimentary basins (e.g. at B2 in NH973-1) (Fig.6).

The deep reflectors (indicated by M-reflectors in Fig.6~Fig.9) below the basement are generally unclear at portions of rugged basement, probably resulting from the serious scatter of the seismic signal or no reflector is actually there. But they are usually imaged below thick sedimentary basins (indicated by B1-B5 in NH973-1 and B1-B8 in CFCST-MCS2013) where the basement is relatively flat. In the northwestern section (CDP 6000-9000 and 11000-18000) of NH973-1 (Fig.6), M-reflectors are clearly seen at depths of 8-9.5 km as a group of intermittent and diffusive reflections. In the southeastern section (CDP 26000-34000) of NH973-1 (Fig.7), the diffusive M-reflectors appear less clearly at depths of 8-9 km. In addition, the M-reflectors deepen to the northwest (continent-ward) around the north continent-ocean transition (COT) (Fig.6), and it is invisible around the south COT of NH973-1 (Fig.5). Similarly, the M-reflectors are seen intermittently and diffusively at depths of 6.5-8.5 km in the northwestern section (CDP 36500-34000 and 31500-29000) and the southeastern section (CDP 17500-10000) of CFCST-MCS2013, more distinct and continuous in the northwestern section (Fig.8~Fig.9). Remarkably, some of the deep normal faults extend down to the level of M-reflectors (e.g. at B2-B5 in NH973-1 and B1-B2 in CFCST-MCS2013) (Fig.6~Fig.9). Additionally, a deep-penetrating fault even cuts off the M-reflectors and extends downwards at B2 in CFCST-MCS2013 (Fig.8).

4.2 Velocity model of OBS973

After 30 iterations, the final velocity model of line OBS973 presented in Figure 10d gets the lowest final root mean square (RMS) residual of 31 ms and reduced χ^2 of 1.91 among a total of 5702 first arrival picks. The modeled travel times fit well with our picked arrivals for the whole profile (Figure 10b). Generally, the refracted ray coverage is dense in most places of the basin area (50~100 km and 145~330 km), giving good constrains on the velocity in these places. However, the ray density is lower between 100 and 145 km, especially below the depth of 8 km.

The basement interpreted from MCS profile NH973-1 is projected to the final velocity model of OBS973 (Fig.10d). Generally, the velocity of the basement varies from 3.5 km/s to 4.5 km/s (Fig.10d

and Fig.11). The velocity model shows two distinct velocity trends beneath the basement, which are identified based on their common velocity gradients. The upper trend extends to depths of 2-3 km below the basement and exhibits smoothly and rapidly increasing velocities from 3.5-4.5 km/s to 7.0-7.6 km/s with an average velocity gradient of 1.0 /s. Below this upper trend, the velocities increase slowly toward 8.0 km/s with a much lower velocity gradient of 0.1 /s on average (Fig.10d and Fig.11). The velocity isocontour of 8.0 km/s, the approximate velocity of unaltered upper mantle (Minshull et al, 1998), is only locally imaged at 145-150 km, 190-230 km and 300 km (Fig.10d). Notably, the velocity increases slowly from 7.2 km/s to 8.0 km/s within a thickness of ~3 km rather than jumps sharply. In addition, the velocities are projected to the corresponding sections of MCS profile NH973-1, and the M-reflectors generally follow the velocity contours of 6.8-7.2 km/s (Fig.6-Fig.7).

5. Discussion

5.1 Nature of the M-reflectors

The M-reflectors are the deepest reflections which can be identified from both MCS profiles (Fig.3 and Fig.6-Fig.9). There are two possible hypotheses for those M-reflectors: they could be (1) the boundary between oceanic layer 2 and layer 3, or (2) the reflection seismic Moho (the base of the crust) (Minshull et al, 1998). Each hypothesis will be discussed after the clear definitions of geological and geophysical Moho.

5.1.1 Definitions of geological and geophysical Moho

Before exploring the nature of M-reflectors, clear definitions of the geological and geophysical Moho in oceanic basins are needed. The geological Moho is a petrological boundary between mafic rocks (crust) above and ultramafic rocks (mantle) below. The geophysical Moho obtained by seismic methods includes the reflection and refraction seismic Moho. The reflection seismic Moho usually refers to the reflection from the boundary between the oceanic crust and uppermost mantle. Historically, the 8.0 km/s velocity isocontour defines the refraction seismic Moho (Bibee and Shor, 1976; Minshull et al, 1998; Delescluse et al, 2015; Davy et al, 2016), resulting in two possible geological models for oceanic crust which fit the observed refraction Moho well: (1) the oceanic crust consists of an upper layer 2 of basaltic lavas and dykes and a lower layer 3 of gabbros, beneath which is the upper mantle peridotite (Penrose model) (Penrose Conference on Ophiolites, 1972); (2)

layer 3 consists of partially serpentinized mantle peridotites, and the refraction Moho marks the boundary between serpentinized and unaltered mantle, i.e. a serpentinization front (Hess, 1962; Minshull et al, 1998). The Penrose model has been highly successful at fast and intermediate spreading mid-ocean ridges with rich magma supply (e.g. the EPR, Aghaei et al, 2014), while the latter model may apply to the slow or ultra-slow spreading ridges with poor magma supply (e.g. the SWIR and MAR, Minshull et al, 1998; Schroeder et al, 2007).

5.1.2 Layer 2/3 boundary hypothesis

Generally, the normal oceanic crustal structure compiled from the Pacific and Atlantic oceans consists of a ~2 km thick layer 2 and a 3-5 km thick layer 3. The velocity in layer 2 increases from ~3 km/s to 6.4 km/s with a large velocity gradient of ~1 /s, while the velocity in layer 3 increases from 6.4 km/s at the top to 7.2 km/s at the base with a much smaller velocity gradient (White et al, 1992). In our MCS profile NH973-1, the M-reflectors mainly follow the 6.8-7.2 km/s velocity contours (Fig.6d and Fig.7d). Such velocities are much close to the velocity at the base of layer 3, but too high for the layer 2/3 boundary. If they were reflections from layer 2/3 boundary, we would expect to see a Moho reflection beneath. In addition, the layer 2/3 boundary has also been barely seen from the MCS profiles in oceanic basins, such as the Pacific ocean (Tsuji et al, 2007; Aghaei et al, 2014) and the ESB and NWSB of the SCS (McIntosh et al, 2014; Cameselle et al, 2015; Sun et al, 2016), since there is usually no distinct velocity jump between layer 2 and layer 3. Therefore, it is unlikely that the M-reflectors in our profiles are the reflections from the layer 2/3 boundary.

5.1.3 Reflection seismic Moho hypothesis

The velocities of these M-reflectors (6.8-7.2 km/s) are much close to the typical velocity of 7.0-7.2 km/s in the base of oceanic crust (White et al, 1992), opening the possibility that they represent the reflection Moho. However, in the final velocity model of OBS973, there is a high velocity transition zone (~3 km thick) from 7.2 km/s to 8.0 km/s (the refraction Moho) beneath these M-reflectors (Fig.10d) rather than a velocity jump boundary, which are consistent with the barely seen PmP arrivals in the OBS observations of the SWSB (Qiu et al, 2011; Pichot et al, 2014; Yu et al, 2016). The velocities of 7.2-8.0 km/s are above the normal upper limit for oceanic crust (7.2 km/s), but too low for unaltered mantle. Such high velocities have been interpreted as due to serpentinization of the upper mantle in fracture zones (Detrick et al, 1993), the COT of non-volcanic rifted margins (Davy et al, 2016), and slow or ultraslow spreading oceanic basins (e.g. the Labrador

11

Sea, Osler and Louden, 1992, 1995; Delescluse et al, 2015). Serpentinization of the upper mantle is facilitated if the magmatic crust is thin, the upper mantle is cool, and there are available pathways for seawater to reach the upper mantle (Minshull et al, 1998; Shillington et al, 2006; Sauter et al, 2013). In the SWSB of the SCS, the MCS profiles NH973-1 and CFCST-MCS2013 show pervasive deep-penetrating faults and anomalously thin and highly fractured oceanic crust (1.5-3.6 km) if the M-reflectors are reflection Moho (Fig.6-Fig.9), providing favorable conditions for serpentinization of the upper mantle rocks with water infiltration along these crustal faults. Velocities from our model sit outside the envelope for Atlantic oceanic crust aged 0-127 Ma at depths >2 km below the top basement, but agree strongly with the velocities profiles through the models of thin oceanic crust overlying serpentinized mantle in the North Atlantic Ocean (Fig.11) (Whitmarsh et al, 1996; Funck et al, 2003; Hopper et al, 2004; Davy et al, 2016). In addition, serpentinization could decrease the velocity and density of the mantle rocks (Rouméjon et al, 2015) and narrow the contrast of wave impedance between oceanic crust and uppermost mantle. As a result, serpentinization may also explain the intermittent or unclear reflection Moho, e.g. at CDP 11000-15000 of NH973-1 (Fig.6) and CDP 32000-28000 of CFCST-MCS2013 (Fig.8). Therefore, it is likely that the M-reflectors in our MCS profiles are the reflection Moho, underlain by the partially serpentinized mantle rocks. In this case, the refraction Moho (8.0 km/s isocontour) represents a serpentinization front.

5.2 Fossil spreading center morphology

The fossil spreading center of the SWSB features spatially varying geomorphological characteristics in different segments (S1, S2, S3 in Fig.1) and is covered by abundant sediments in S2 and S3 (Li et al, 2012; Ding et al, 2016). In the free air gravity anomaly (FAA) map, it appears as an obvious low value zone (Braitenberg et al, 2006; Li et al, 2013), which is the typical feature of a median valley. The median valley in CFCST-MCS2013 (Fig.5b) is occupied by an isolated abnormal seamount (Longmen Seamount) (Fig.2) where FAA remains low (Wang et al, 2017). In NH973-1, the median valley covered by sediments up to 3.3 km thick is more obvious and ~ 40 km wide (Fig.12a).

For most ocean and seas, mid-ridge morphology seems to be correlative with magma supply. At the magma-rich ridge, the axial morphology is usually characterized by an elevated volcanic edifice (> 500 m high), such as the fast-spreading East Pacific Rise (EPR) (Fig.12d) (Aghaei et al, 2014) and the Michelson Ridge in the Western Pacific (Tsuji et al, 2007). On the contrary, there is always a median valley (> 1 km deep) within the magma-poor ridges, e.g. the slow spreading 15°N

Mid-Atlantic Ridge (MAR) (Fig.12c) (Schroeder et al, 2007) and the ultra-slow spreading Southwest Indian Ridge (SWIR) (Fig.12b) (Cannat et al, 2006). In the SWSB, the fossil spreading ridge is significantly different from magma-rich ridges, and should be a magma-poor ridge.

5.3 Tectonism-dominant seafloor spreading in the SWSB

Our main constrain on the magma supply from the melt mantle at mid-ocean ridges is the thickness of oceanic crust determined by seismic methods (Minshull et al, 1998). At magma-rich seafloor spreading ridges, the oceanic crust is generally thick (> 5.5 km, averaging 7.1 km; White et al, 1992). For example, the thickness of oceanic crust is about 6 km on both sides of the Michelson ridge in the eastern Ogasawara Plateau region (Tsuji et al, 2007); the average thickness of the new oceanic crust is 5740 ±270 m at the fast-spreading EPR from 9°42'N to 9°57'N (Aghaei et al, 2014). In contrast, the oceanic crust of magma-poor seafloor spreading is generally thin (<5 km) or even absent, and the upper mantle might be partially serpentinized or even exhumed to the seafloor. For example, the oceanic crust is only 3-4 km off the Newfoundland in the North Atlantic Ocean (Hopper et al, 2004), 1.5-5 km in the extinct Labrador Sea (Delescluse et al, 2015), and absent with the mantle rocks directly exposed to the seafloor in the 15°N MAR (Schroeder et al, 2007) and the SWIR (Cannat et al, 2006).

In the SWSB of the SCS, the intermittent and diffusive M-reflectors are clearly imaged beneath the main sedimentary basins (B1-B5 in NH973-1 and B1-B8 in CFCST-MCS2013) in the oceanic domain (Fig.6-Fig.9). As discussed above, these M-reflectors probably represent the reflection seismic Moho, thus the thickness of the crust (excluding the sediment) is only 1.5-3.6 km, much thinner than the normal oceanic crust (averaging 7.1 km thick; White et al, 1992) but close to the oceanic crustal thickness in magma-poor spreading basins, e.g. the North Atlantic Ocean (Hopper et al, 2004) and extinct Labrador Sea (Delescluse et al, 2015), indicating the poor magma supply during seafloor spreading. Meanwhile, numerous deep normal faults cut the basement into many different blocks, leading to the formation of rough basement and a series of local deep sedimentary basins (Fig.6-Fig.9) (Li et al, 2012; Ding et al, 2016). Such thin crust, widely distributed deep-penetrating faults, highly faulted basement blocks and local deep sedimentary basins all indicate that the SWSB of the SCS has experienced strong tectonic extension. This strong tectonic extension involves both syn-spreading and post-spreading extensions. However, the sedimentary sequences are mostly sub-horizontal with very limited syn-tectonic sedimentary wedges (Fig.6-Fig.9) (Ding et al, 2016)

and the young normal faults are shallow and weak, so we can infer that the post-spreading extension is limited and the syn-spreading extension plays a leading role in generating the highly fractured and anomalously thin crust in the SWSB. In addition, Qiu et al. (2008) proposed that fresh late Early Cretaceous granite rocks dredged from the SWSB (Dredge site 3yDG in Fig.2) are comparable to Mesozoic granites in the southeastern China and may be the rafted residual continental rocks during seafloor spreading. This further supports that the syn-spreading magmatism was weak, otherwise the continent-affinity rocks would be altered. Therefore, the development of the SWSB was tectonism-dominant and in a magma-poor setting.

However, the oceanic crustal structures of the ESB and NWSB are quite different from those of the SWSB, probably resulting from different dynamic origins of the seafloor spreading in those sub-basins. Although the fossil spreading center of the NWSB is featureless and unidentified, it is non-negative (Fig.1; Cameselle et al, 2015). The ESB shows positive mid-ridge in bathymetric map (Fig.1). Viewing from the MCS profiles in the ESB and NWSB (McIntosh et al, 2014; Cameselle et al, 2015; Sun et al, 2016), the oceanic basement is fairly flat with limited minor normal faults, the reflection Moho is clear and relatively continuous, and the oceanic crust is quite uniform and thick (averaging 6.0 km). These crustal features are comparable to those of typical oceanic crust created by magmatism-dominant seafloor spreading (White et al, 1992; Tsuji et al, 2007; Aghaei et al, 2014). Therefore, the seafloor spreading was relatively magma-rich in the ESB and NWSB, while magma-poor in the SWSB. This further supports the east to west propagation of South China Sea opening (Briais et al, 1993; Cullen et al, 2010), which cannot be explained by the rotation and extrusion of the Indochina Peninsula (Tapponnier et al, 1982, 1986). In summary, magmatism dominated the seafloor spreading in the east of the SCS after the breakup of the South China continent, then magma supply decreased with the southwestern propagation of the seafloor spreading and the tectonic extension played a dominant role in the seafloor spreading of the southwestern part of the SCS.

6. Conclusions

（1） In middle segment of the SWSB, the deep reflections are imaged as a group of intermittent and diffusive reflectors at 1.5-3.6 km beneath the thick sedimentary basins in oceanic domain of both MCS profiles. The deep reflectors in MCS profile NH973-1 follow the velocity

contours of 6.8-7.2 km/s, indicating that they might mark the base of the crust. Thus the crustal thickness is only 1.5-3.6 km excluding sediments, much thinner than the typical oceanic crust.

（2）The high velocity layer below this thin crust in OBS973 might be the serpentinized uppermost mantle with velocities gradually increasing to 8.0 km/s with depth. Thin oceanic crust and widely distributed deep-penetrating faults in the basin area are suggested to facilitate the serpentinization and indicate that the Southwest Sub-basin has experienced significant tectonic extension.

（3）The SWSB originated from tectonism-dominant seafloor spreading with poor magma supply, while the seafloor spreading in the ESB and NWSB was relatively magma-rich. The magma supply decreased with the southwestern propagation of the seafloor spreading from the eastern part of the SCS.

References

Aghaei, O., Nedimović, M.R., Carton, H., Carbotte, S.M., Canales, J.P., Mutter, J.C., 2014. Crustal thickness and Moho character of the fast-spreading East Pacific Rise from 9 42'N to 9 57'N from poststack-migrated 3-D MCS data. Geochemistry, Geophysics, Geosystems 15 (3), 634-657.

Barckhausen, U., Roeser, H.A., 2004. Seafloor spreading anomalies in the South China Sea revisited. In: Clift, P., Kuhnt, W., Wang, P., Hayes, D.E. (Ed.), Continent-ocean Interactions in the East Asian Marginal Seas. American Geophysical Union, Washington, D. C., pp. 121-125.

Bibee, L.D., Shor, G.G., 1976. Compressional wave anisotropy in the crust and upper mantle. Geophysical Research Letters 3, 639-642.

448 Braitenberg, C., Wienecke, S., Wang, Y., 2006. Basement structures from satellite-derived gravity
449   field: South China Sea ridge. Journal of Geophysical Research: Solid Earth 111, B05407, 1-15.

450 Briais, A., Patriat, P., Tapponnier, P., 1993. Updated interpretation of magnetic anomalies and
451   seafloor spreading stages in the south China Sea: Implications for the Tertiary tectonics of
452   Southeast Asia. Journal of Geophysical Research 98 (B4), 6299-6328.

453 Cameselle, A.L., Ranero, C.R., Franke, D., Barckhausen, U., 2015. The continent-ocean transition on
454   the northwestern South China Sea. Basin Research 17, 1-23.

455 Cannat, M., Sauter, D., Mendel, V., Ruellan, E., Okino, K., Escartin, J., Combier, V., Baala, M., 2006.
456   Modes of seafloor generation at a melt-poor ultraslow-spreading ridge. Geology 34 (7),
457   605-608.

458 Carton, H., Singh, S.C., Hananto, N.D., Martin, J., Djajadihardja, Y.S., Udrekh, Franke, D., Gaedicke,
459   C., 2014. Deep seismic reflection images of the Wharton Basin oceanic crust and uppermost
460   mantle offshore Northern Sumatra: Relation with active and past deformation. Journal of
461   Geophysical Research: Solid Earth 119, 32-51.

462 Collins, J.A., Purdy, M.G., Brocher, T.M., 1989. Seismic velocity structure at Deep Sea Drilling
463   Project site 504B, Panama Basin: Evidence for thin oceanic crust. Journal of Geophysical
464   Research 94 (B7), 9283-9302.

465 Cullen, A., Reemst, P., Henstra, G., Gozzard, S., Ray, A., 2010. Rifting of the South China Sea: new
466   perspectives. Petroleum Geoscience 16, 273-282.

467 Davy, R.G., Minshull, T.A., Bayrakci, G., Bull, J.M., Klaeschen, D., Papenberg, C., Reston, T.J.,
468   Sawyer, D.S., Zelt, C.A., 2016. Continental hyperextension, mantle exhumation, and thin
469   oceanic crust at the continent-ocean transition, West Iberia: New insights from wide-angle
470   seismic. Journal of Geophysical Research: Solid Earth 121, 3177-3199.

471 Dean, S.L., Sawyer, D.S., Morgan, J.K., 2015. Galicia Bank ocean–continent transition zone: New
472   seismic reflection constraints. Earth and Planetary Science Letters 413, 197-207.

473 Delescluse, M., Funck, T., Dehler, S.A., Louden, K.E., Watremez, L., 2015. The oceanic crustal
474   structure at the extinct, slow to ultraslow Labrador Sea spreading center. Journal of Geophysical
475   Research: Solid Earth 120, 5249-5272.

476 Detrick, R.S., White, R.S., Purdy, G.M., 1993. Crustal structure of North Atlantic fracture zones.
477   Reviews of Geophysics 31 (4), 439-458.

Dick, H.J.B., Lin, J., Schouten, H., 2003. An ultraslow-spreading class of ocean ridge. Nature 426, 405-412.

Dick, H.J.B., MacLeod, C.J., Blum, P., and the Expedition 360 Scientists, 2016. Expedition 360 Preliminary Report: Southwest Indian Ridge lower crust and Moho. International Ocean Discovery Program, doi: 10.14379/iodp.pr.360.2016.

Ding, W.W., Franke, D., Li, J.B., Steuer, S., 2013. Seismic stratigraphy and tectonic structure from a composite multi-channel seismic profile across the entire Dangerous Grounds, South China Sea. Tectonophysics 582, 162-176.

Ding, W.W., Li, J.B., Clift, P.D., IODP Expedition 349 Scientists, 2016. Spreading dynamics and sedimentary process of the Southwest Sub-basin, South China Sea: Constraints from multi-channel seismic data and IODP Expedition 349. Journal of Asian Earth Sciences 115, 97-113.

Expedition 349 Scientists, 2014. South China Sea tectonics: opening of the South China Sea and its implications for southeast Asian tectonics, climates, and deep mantle processes since the late Mesozoic. International Ocean Discovery Program Preliminary Report, 349, doi: 10.14379/iodp.pr.349.2014.

Franke, D., Savva, D., Pubellier, M., Steuer, S., Mouly, B., Auxietre, J.-L., Meresse, F., Chamot-Rooke, N., 2014. The final rifting evolution in the South China Sea. Marine and Petroleum Geology 58, 704-720.

Funck, T., Hopper, J.R., Larsen, H.C., Louden, K.E., Tucholke, B.E., Holbrook, W.S., 2003. Crustal structure of the ocean-continent transition at Flemish Cap: Seismic refraction results. Journal of Geophysical Research 108 (B11), 2531.

Grindlay, N.R., Madsen, J.A., Rommevaux-Jestin, C., Sclater, J., 1998. A different pattern of ridge segmentation and mantle Bouguer gravity anomalies along the ultra-slow spreading Southwest Indian Ridge (15°30′E to 25°E). Earth and Planetary Science Letters 161, 243-253.

Hall, R., 2002. Cenozoic geological and plate tectonic evolution of SE Asia and the SW Pacific: computer-based reconstructions, model and animations. Journal of Asian Earth Sciences 20, 353-431.

Hall, R., 2009. Hydrocarbon basins in SE Asia: understanding why they are there. Petroleum Geoscience 15, 131-146.

Hayes, D.E., Nissen, S.S., 2005. The south China Sea margins: implication for rifting contrast. Earth and Planetary Science Letters 237, 601-616.

Hess, H.H., 1962. History of ocean basins. In: Engel, A.E., James, H.L. & Leonard, B.F. Petrologic Studies, Burlington Volume. Geological Society of America, Boulder, Colorado, 599-620.

Hobro, J.W.D., Singh, S., Minshull, T.A., 2003. Three-dimensional tomographic inversion of combined reflection and refraction seismic traveltime data. Geophysical Journal International 152, 79-93.

Hopper, J.R., Funck, T., Tucholke, B.E., Christian Larsen, H., Holbrook, W.S., Louden, K.E., Shillington, D., Lau, H., 2004. Continental breakup and the onset of ultraslow seafloor spreading off Flemish Cap on the Newfoundland rifted margin. Geology 32 (1), 93-96.

Huang, C.J., Zhou, D., Sun, Z., Chen, C.M., Hao, H.J., 2005. Deep crustal structure of Baiyun Sag, northern South China Sea revealed from deep seismic reflection profile. Chinese Science Bulletin 50 (11), 1131-1138.

Korenaga, J., Holbrook, W.S., Kent, G.M., Kelemen, P.B., Detrick, R.S., Larsen, H.C., Hopper, J.R., Dahl-Jensen, T., 2000. Crustal structure of the Southeast Greenland margin from joint refraction and reflection seismic tomography. Journal of Geophysical Research 105, 21591-21614.

Li, C.F., Xu, X., Lin, J., Sun, Z., Zhu, J., Yao, Y.J., Zhao, X.X., Liu, Q.S., Kulhanek, D.K., Wang, J., Song, T.R., Zhao, J.F., Qiu, N., Guan, Y.X., Zhou, Z.Y., Williams, T., Bao, R., Briais, A., Brown, E.A., Chen, Y.F., Clift, P.D., Colwell, F.S., Dadd, K.A., Ding, W.W., Almeida, I.H., Huang, X.L., Hyun, S.M., Jiang, T., Koppers, A.A.P., Li, Q.Y., Liu, C.L., Liu, Z.F., Nagai, R.H., Peleo-Alampay, A., Su, X., Tejada, M.L.G., Trinh, H.S., Yeh, Y.C., Zhang, C.L., Zhang, F., Zhang, G.L., 2014. Ages and magnetic structures of the South China Sea constrained by deep tow magnetic surveys and IODP Expedition 349. Geochemistry Geophysics Geosystems 15, 4958-4983.

Li, J.B., Ding, W.W., Wu, Z.Y., Zhang, J.P., Dong, C.Z., 2012. The propagation of seafloor spreading in the southwestern subbasin, South China Sea. Chinese Science Bulletin 57 (24), 3182-3191.

Li, X.B., Wu, Z.L., Li, J.B., 2013. The preliminary study of segmentation of the mid-ocean ridge in Southwest Sub-basin of the South China Sea. Marine Geology & Quaternary Geology 33 (3), 101-107 (in Chinese with English Abstract).

Liu, Y.B., Yu, H., 2009. Report on seismic data processing of 2-D survey lines in the south China Sea

(in Chinese).

Lü, C.C., Hao, T.Y., Qiu, X.L., Zhao, M.H., You, Q.Y., 2011. A study on the deep structure of the northern part of Southwest sub-basin from ocean bottom seismic data, South China Sea. Chinese Journal of Geophysics 54 (12), 3129-3138 (in Chinese with English Abstract).

McIntosh, K., Lavier, L., van Avendonk, H., Lester, R., Eakin, D., Liu, C.-S., 2014. Crustal structure and inferred rifting processes in the northeast South China Sea. Marine and Petroleum Geology 58, 612-626.

Minshull, T.A., Muller, M.R., Robinson, C.J., White, R.S., Bickle, M.J., 1998. Is the oceanic Moho a serpentinization front? In Modern Ocean Floor Processes and the Geological Record, edited by R. A. Mills and K. Harrison, Geol. Soc. Spec. Publ., London, 148, 71-80.

Muller, M.R., Minshull, T.A., White, R.S., 2000. Crustal structure of the Southwest Indian Ridge at the Atlantis II Fracture Zone. Journal of Geophysical Research Atmospheres 105 (B11), 25809-25828.

Mutter, J.C., Karson, J.A., 1992. Structural processes at slow-spreading ridges. Science 257, 627-634.

Osler, J.C., Louden, K.E., 1992. Crustal structure of an extinct rift axis in the Labrador Sea: Preliminary results from a seismic refraction survey. Earth and Planetary Science Letters 108 (4), 243-258.

Osler, J.C., Louden, K.E., 1995. Extinct spreading center in the Labrador Sea: Crustal structure from a two-dimensional seismic-refraction velocity model. Journal of Geophysical Research 100 (B2), 2261-2278.

Penrose Conference on Ophioloites, 1972. Geotimes 17, 24-25.

Pichot, T., Delescluse, M., Chamot-Rooke, N., Pubellier, M., Qiu, Y., Meresse, F., Sun, G., Savva, D., Wong, K.P., Watremez, L., Auxiètre, J.L., 2014. Deep crustal structure of the conjugate margins of the SW South China Sea from wide-angle refraction seismic data. Marine and Petroleum Geology 58, 627-643.

Pubellier, M., Monnier, C., Maury, R., Tamayo, R., 2004. Plate kinematics, origin and tectonic emplacement of supra-subduction ophiolites in SE Asia. Tectonophysics 392, 9-36.

Qiu, X.L., Zhao, M.H., Ao, W., Lü, C.C., Hao, T.Y., You, Q.Y., Ruan, A.G., Li, J.B., 2011. OBS survey and crustal structure of the Southwest Sub-basin and Nansha Block, South China Sea.

568   Chinese Journal of Geophysics 54 (6), 1009–1021.

569 Qiu, Y., Chen, G.N., Liu, F.L., Peng, Z.L., 2008. Discovery of granite and its tectonic significance in

570   southwestern basin of the South China Sea. Geological Bulletin of China 27 (12), 2104-2107 (in

571   Chinese with English Abstract).

572 Roumégon, S., Cannat, M., Agrinier, P., Godard, M., Andreani, M., 2015. Serpentinization and Fluid

573   Pathways in Tectonically Exhumed Peridotites from the Southwest Indian Ridge (62–65°E).

574   Journal of Petrology 56 (4), 703-734.

575 Sauter, D., Cannat, M., Roumégon, S., Andreani, M., Birot, D., Bronner, A., Brunelli, D., Carlut, J.,

576   Delacour, A., Guyader, V., 2013. Continuous exhumation of mantle-derived rocks at the

577   Southwest Indian Ridge for 11 million years. Nature Geoscience 6, 314-320.

578 Savva, D., Meresse, F., Pubellier, M., Chamot-Rooke, N., Lavier, L., Po, K.W., Franke, D., Steuer, S.,

579   Sapin, F., Auxietre, J.L., Lamy, G., 2013. Seismic evidence of hyper-stretched crust and mantle

580   exhumation offshore Vietnam. Tectonophysics 608, 72-83.

581 Schroeder, T., Cheadle, M.J., Dick, H.J.B., Faul, U., Casey, J.F., Kelemen, P.B., 2007. Nonvolcanic

582   seafloor spreading and corner-flow rotation accommodated by extensional faulting at 15°N on

583   the Mid-Atlantic Ridge: A structural synthesis of ODP Leg 209. Geochemistry Geophysics

584   Geosystems 8 (6), 623-636.

585 Shillington, D.J., Holbrook, W.S., Van Avendonk, H.J.A., Tucholke, B.E., Hopper, J.R., Louden, K.E.,

586   Larsen, H.C., Nunes, G.T., 2006. Evidence for asymmetric nonvolcanic rifting and slow

587   incipient oceanic accretion from seismic reflection data on the Newfoundland margin. Journal

588   of Geophysical Research 111, B09402, doi: 09410.01029/02005jb003981.

589 Sleep, N.H., Barth, G.A., 1997. The nature of oceanic lower crust and shallow mantle emplaced at

590   low spreading rates. Tectonophysics 279, 181-191.

591 Song, T., Li, C.-F., 2015. Rifting to drifting transition of the Southwest Subbasin of the South China

592   Sea. Marine Geophysical Research 36, 167-185.

593 Srivastava, S.P., Keen, C.E., 1995. A deep seismic-reflection profile across the extinct Mid-Labrador

594   sea spreading center. Tectonics 14 (2), 372-389.

595 Sun, Z., Stock, J., Jian, Z.M., McIntosh, K., Alvarez-Zarikian, C.A., Klaus, A., 2016. Expedition

596   367/368 Scientific Prospectus: South China Sea Rifted Margin. International Ocean Discovery

597   Program, doi: 10.14379/iodp.sp.367368.2016.

598 Tapponnier, P., Peltzer, G., Armijo, R., 1986. On the Mechanics of the collision Between India and

599 Asia. In: Geological Society of London Special Publication, 19, 115-157.

600 Tapponnier, P., Peltzer, G., Le Dain, A.Y., Armijo, R., Cobbold, P., 1982. Propagating extrusion

601 tectonics in Asia: new insights from simple experiments with plasticine. Geology 10, 611-616.

602 Taylor, B., Hayes, D.E., 1983. Origin and history of the South China Sea basin. In: Hayes, D.E. (Ed.),

603 The Tectonic and Geologic Evolution of Southeast Asian Seas and Islands, Geophysical

604 Monograph. American Geophysical Union, Washington, D. C., pp. 23-56.

605 Tsuji, T., Nakamura, Y., Tokuyama, H., Coffin, M.F., Koda, K., 2007. Oceanic crust and Moho of the

606 Pacific Plate in the eastern Ogasawara Plateau region. Island Arc 16, 361-373.

607 Wang, X.J., Wu, M.Q., Liang, D.H., Yin, A.W., 1985. Some geochemical characteristics of basalts in

608 the South China Sea. Acta Geochimica 4 (4), 380-390.

609 Wang, Y.L., Wang, J., Yan, P., Qiu, Y., 2017. An Anomalous Seamount on the Southwestern

610 Mid-Ridge of the South China Sea. ACTA GEOLOGICA SINICA (English Edition) 91 (6),

611 1141-1142.

612 White, R.S., McKenzie, D., O'Nions, R.K., 1992. Oceanic crustal thickness from seismic

613 measurements and rare earth element inversions. Journal of Geophysical Research 97 (B13),

614 19683-19715.

615 Whitmarsh, R.B., White, R.S., Horsefield, S.J., Sibuet, J.C., Recq, M., Louvel, V., 1996. The

616 ocean-continent boundary off the western continental margin of Iberia: Crustal structure west of

617 Galicia Bank. Journal of Geophysical Research 101, 28291-28314.

618 Yan, P., Deng, H., Liu, H.L., Zhang, Z.R., Jiang, Y.K., 2006. The temporal and spatial distribution of

619 volcanism in the South China Sea region. Journal of Asian Earth Sciences 27, 647-659.

620 Yan, P., Zhou, D., Liu, Z.S., 2001. A crustal structure profile across the northern continental margin

621 of the South China Sea. Tectonophysics 338, 1-21.

622 Yan, Q.S., Shi, X.F., Castillo, P.R., 2014. The late Mesozoic–Cenozoic tectonic evolution of the

623 South China Sea: A petrologic perspective. Journal of Asian Earth Sciences 85, 178-201.

624 Yan, Q.S., Shi, X.F., Yang, Y.M., Wang, K.S., 2008. K-Ar/Ar-Ar Geochronology of Cenozoic alkali

625 basalts from the South China Sea. Acta Oceanologica Sinica 27 (6), 115-123.

626 Yang, S.X., Qiu, Y., Zhu, B.D., Chen, J., Guan, Y.X., Peng, X.C., Gao, H.F., Guo, L.H., Huang, W.X.,

627 Wang, J., Zhong, H.X., Cui, X.Y., Wan, R.S., Liu, L.Q., Zhang, H.D., Tang, J.L., Zhang, J.P.,

628   Cai, G.Q., Sun, G.H., Han, B., Du, D.L., Deng, H.R., Liu, S.X., Li, G., Lü, W.C., 2015. Atlas of
629   geology and geophysics of the south china sea. China Navigation Publications, Tianjin.

630 Yu, J.H., Yan, P., Zheng, H.B., Wang, Y.L., Zhao, X., 2017. Imaging of reflection Moho in the
631   Southwest Sub-basin of South China Sea and its geological implications. Marine Geology &
632   Quaternary Geology 37 (2), 75-81 (in Chinese with English Abstract).

633 Yu, Z.T., Li, J.B., Ding, W.W., Zhang, J., Ruan, A.G., Niu, X.W., 2016. Crustal structure of the
634   Southwest Subbasin, South China Sea, from wide-angle seismic tomography and seismic
635   reflection imaging. Marine Geophysical Research, doi:10.1007/s11001-11016-19284-11001.

636 Zelt, C., Barton, P., 1998. Three-dimensional seismic refraction tomography: A comparison of two
637   methods applied to data from the Faeroe Basin. Journal of Geophysical Research 103 (B4),
638   7187-7210.

639 Zelt, C.A., Smith, R.B., 1992. Seismic traveltime inversion for 2-D crustal velocity structure.
640   Geophysical Journal International 108 (1), 16-34.

641 Zhang, J., Li, J.B., Ruan, A.G., Wu, Z.L., Yu, Z.T., Niu, X.W., Ding, W.W., 2016. The velocity
642   structure of a fossil spreading centre in the Southwest Sub-basin, South China Sea. Geological
643   Journal 51, 548-561.

644 Zhao, C.Y., Song, H.B., Li, J.B., Song, Y., Tian, L.H., 2011. Tectonic and seismic interpretation of
645   line NH973-1 along southwest sub-basin in South China Sea. Chinese Journal of Geophysics 54
646   (12), 3258-3268 (in Chinese with English Abstract).

647
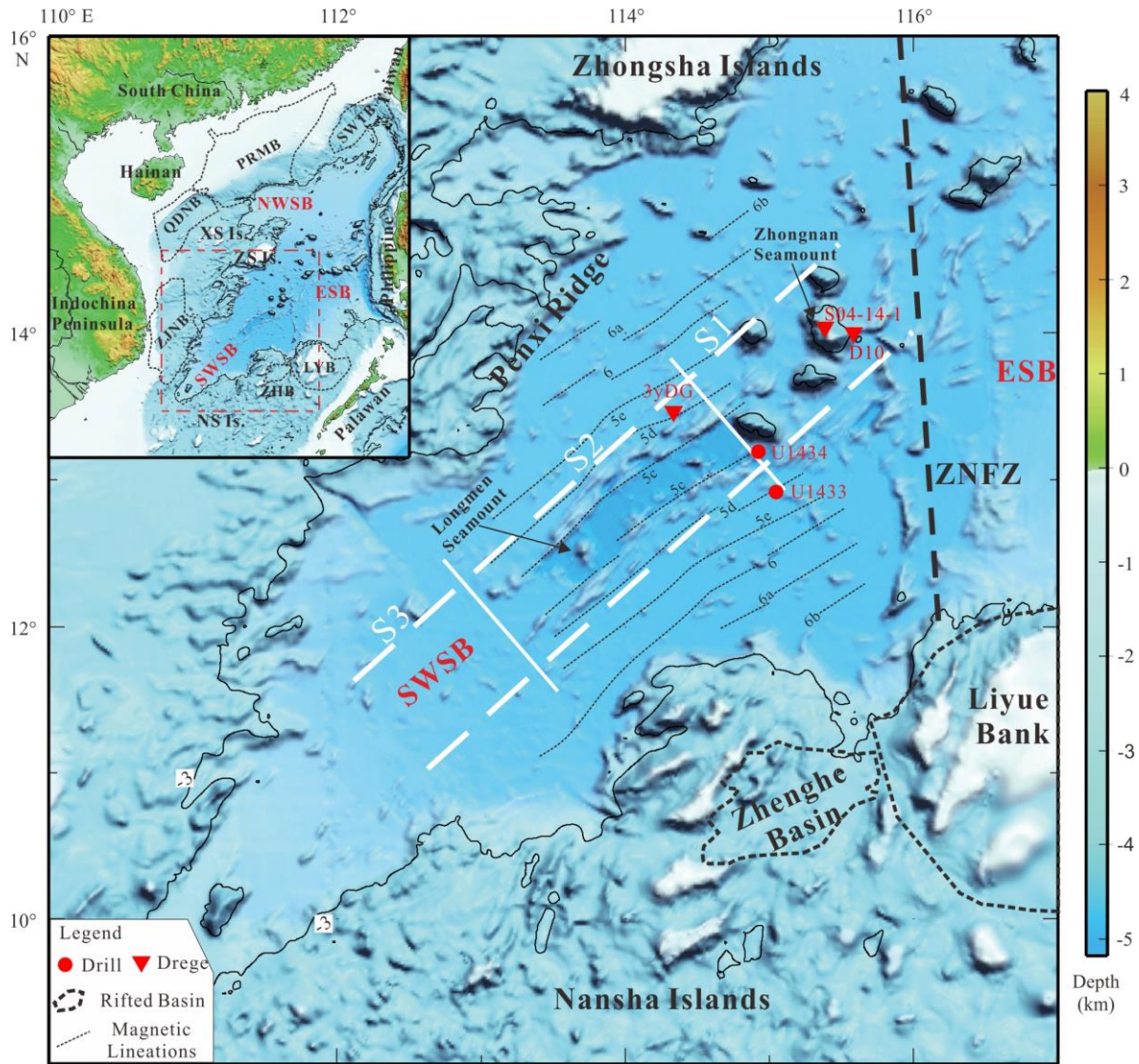
Fig.1. Bathymetric map of the Southwest Sub-basin, South China Sea. The base map is modified from Yang et al, 2015. Drilling sites (U1433 and U1434) of IODP Expedition 349 are indicated by red dots. Red triangles indicate the dredge sites: 3yDG (Qiu et al, 2008), S04-14-1 and D10 (Yan et al, 2014). The thick black dashed line shows the boundary between the East Sub-basin and the Southwest Sub-basin. The interpreted magnetic anomalies shown in thin black dashed lines are from Briais et al, 1993. The fossil spreading center is bounded by the white dashed lines. NWSB: the Northwest Sub-basin; ESB: the East Sub-basin; SWSB: the Southwest Sub-basin; ZNFZ: Zhongnan Fracture Zone; XS Is.: Xisha Islands; ZS Is.: Zhongsha Islands; NS Is.: Nansha Islands; SWTB: Southwest Taiwan basin; PRMB: Pearl River Mouth basin; QDNB: Qiongdongnan basin; ZJNB: Zhongjiannan basin; ZHB: Zhenghe basin; LYB: Liyue basin.
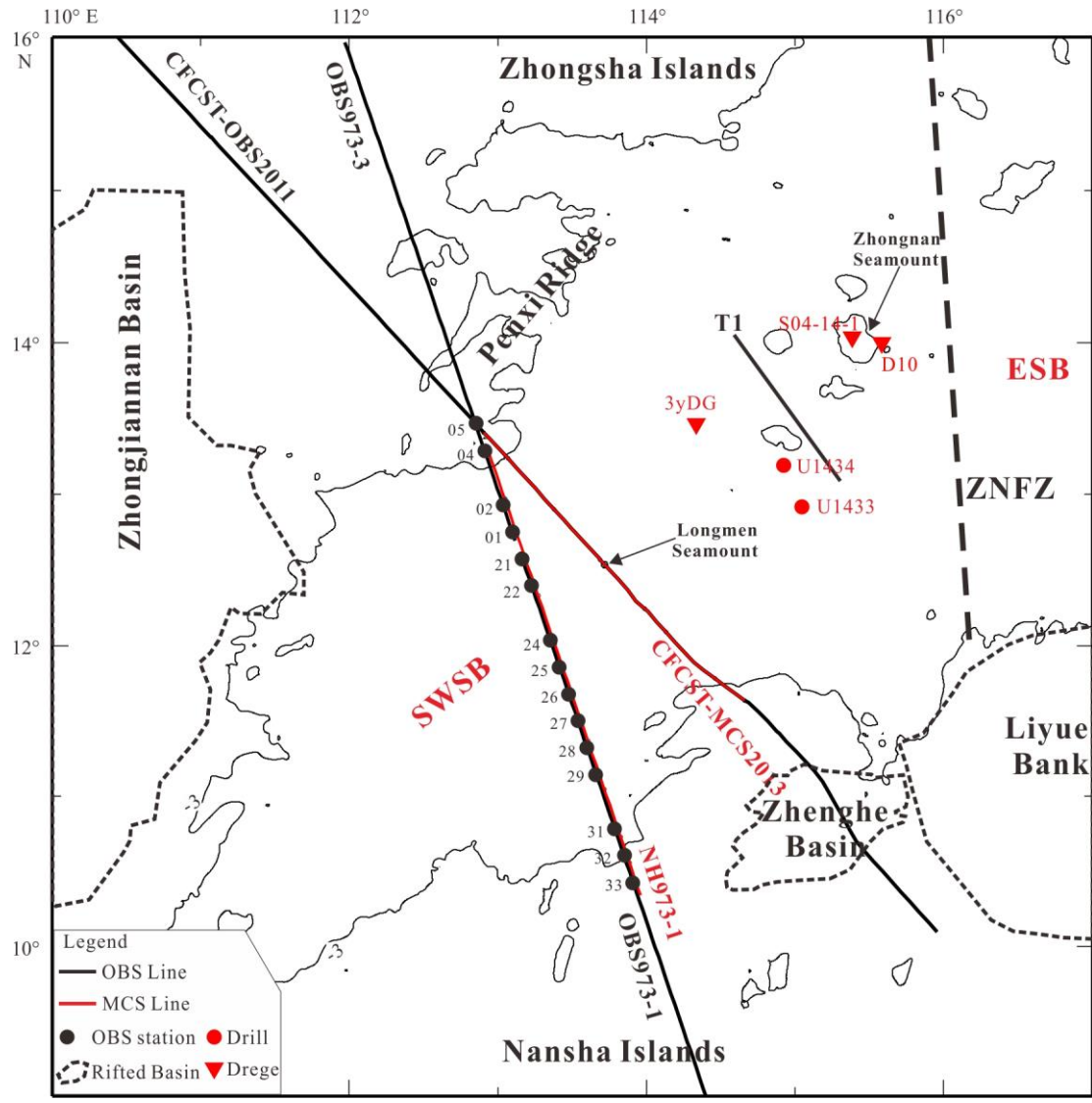
Fig.2. Location map of the seismic survey lines across the Southwest Sub-basin. The blacks lines indicate the OBS lines: OBS973-1 (Qiu et al, 2011), OBS973-3 (Lü et al, 2011), CFCST-OBS2011 (Pichot et al, 2014) and T1 (Zhang et al, 2016). The red lines present the coincident MCS sections (NH973-1 and CFCST-MCS2013) we reprocessed. The black dots display the OBS positions of Line OBS973 integrated from OBS973-1 and OBS973-3.
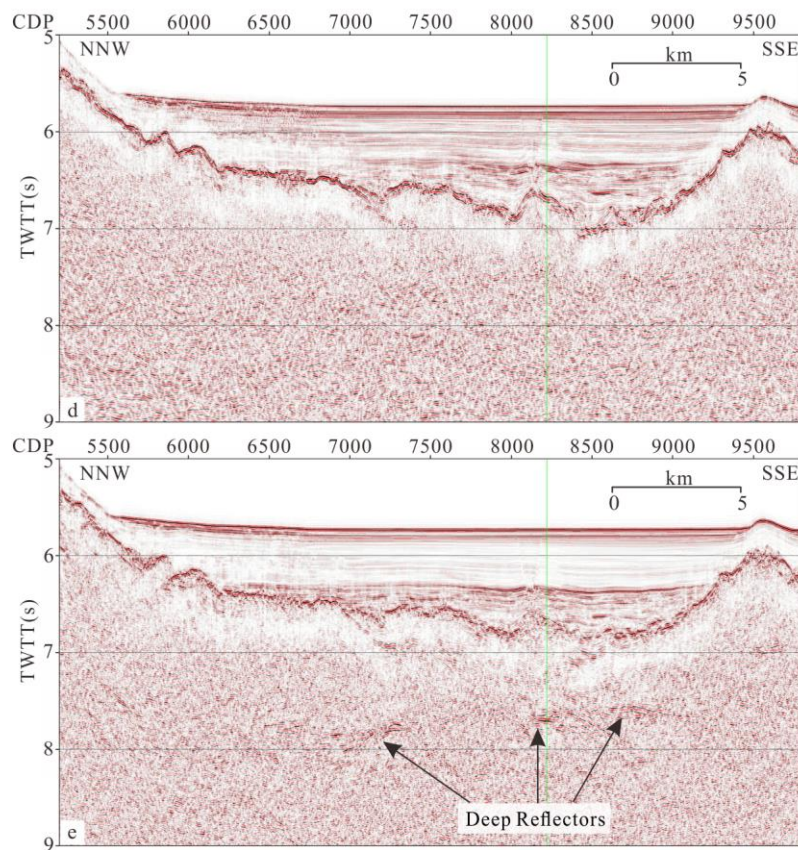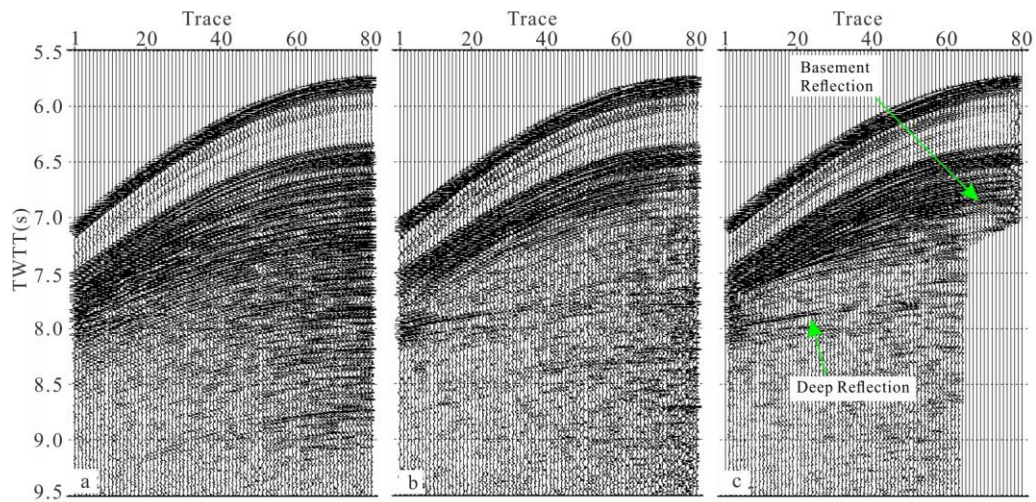
Fig.3. The gather of CDP 8218 before peg-leg multiples attenuation (a), after parabolic Radon

transform filtering (b) and inner muting (c). Comparison of time-migrated section of profile

NH973-1 processed by CNOOC (d) and this study (e). The green lines indicate the location of CDP

8218. The vertical exaggeration in (d, e) is 1.5.

673
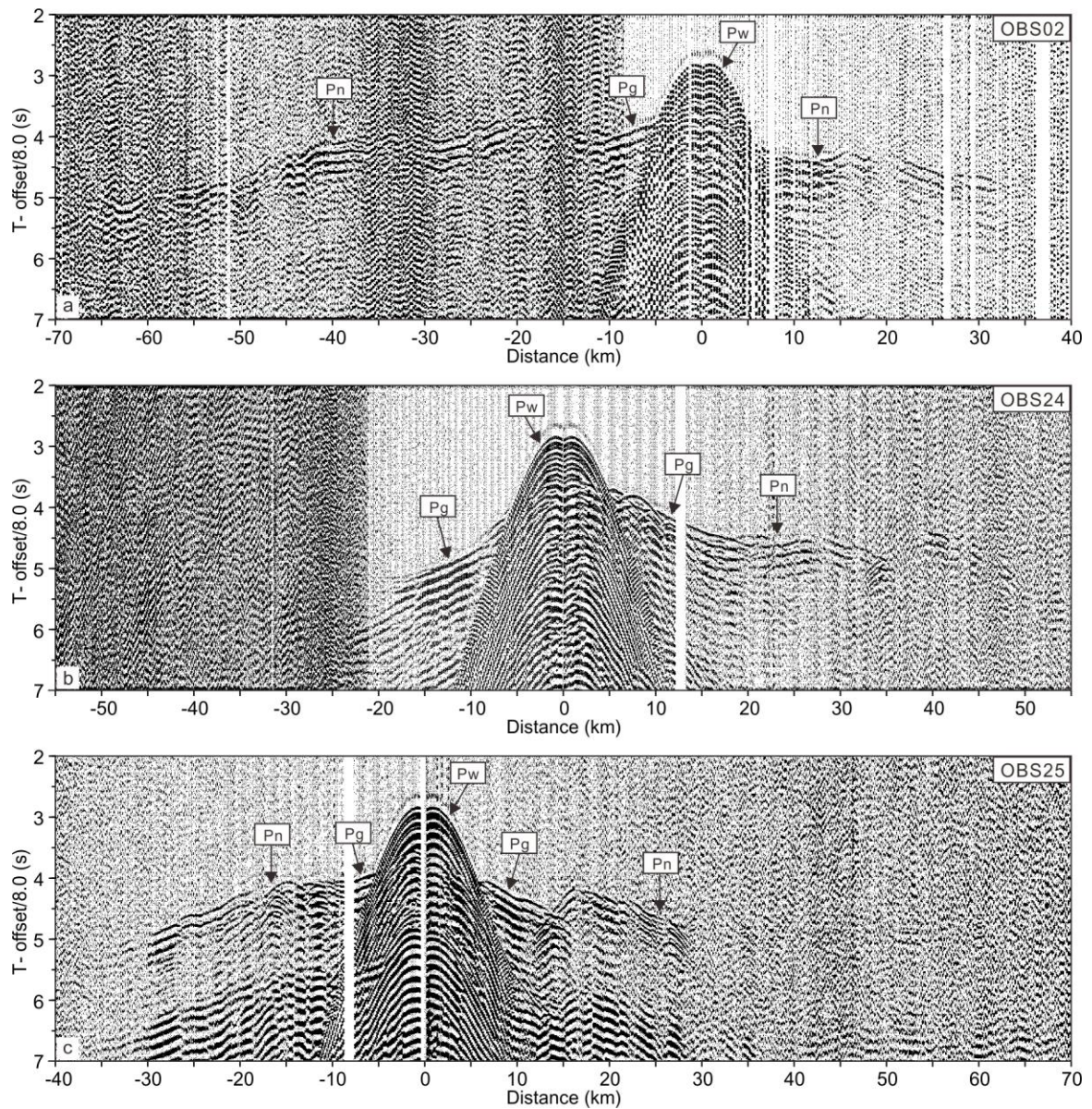
Fig.4. The seismic record profiles of OBS 02 (a), OBS 24 (b) and OBS 25 (c) in the abyssal basin

show poor PmP arrivals. The data are band-pass filtered (5-15 Hz).

676
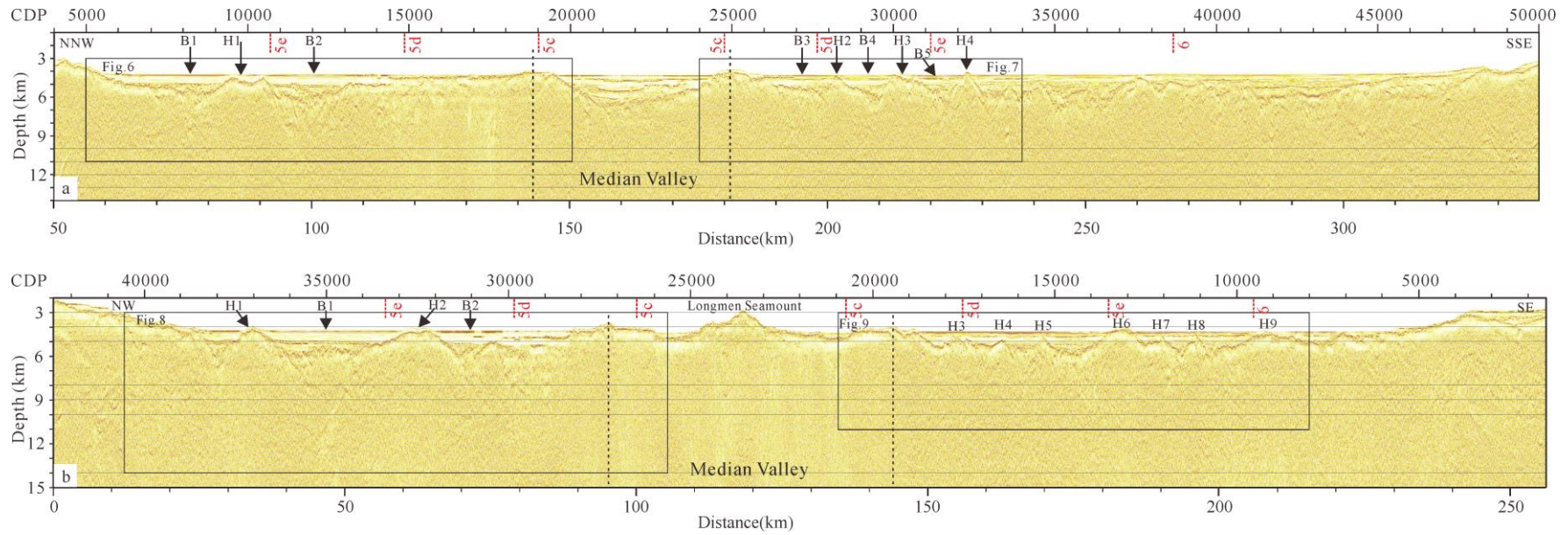
Fig.5. Depth-converted MCS profiles NH973-1 (a) and CFCST-MCS2013 (b) over the Southwest sub-basin. The magnetic lineations interpreted by Briais et al, 1993 are shown in red dashed lines. Letters indicated by arrows designate specific features discussed in the text. The black dashed lines indicate the rift shoulders. The black boxes are further shown in Fig.6-9. Vertical exaggeration in (b, d) is 2.5.
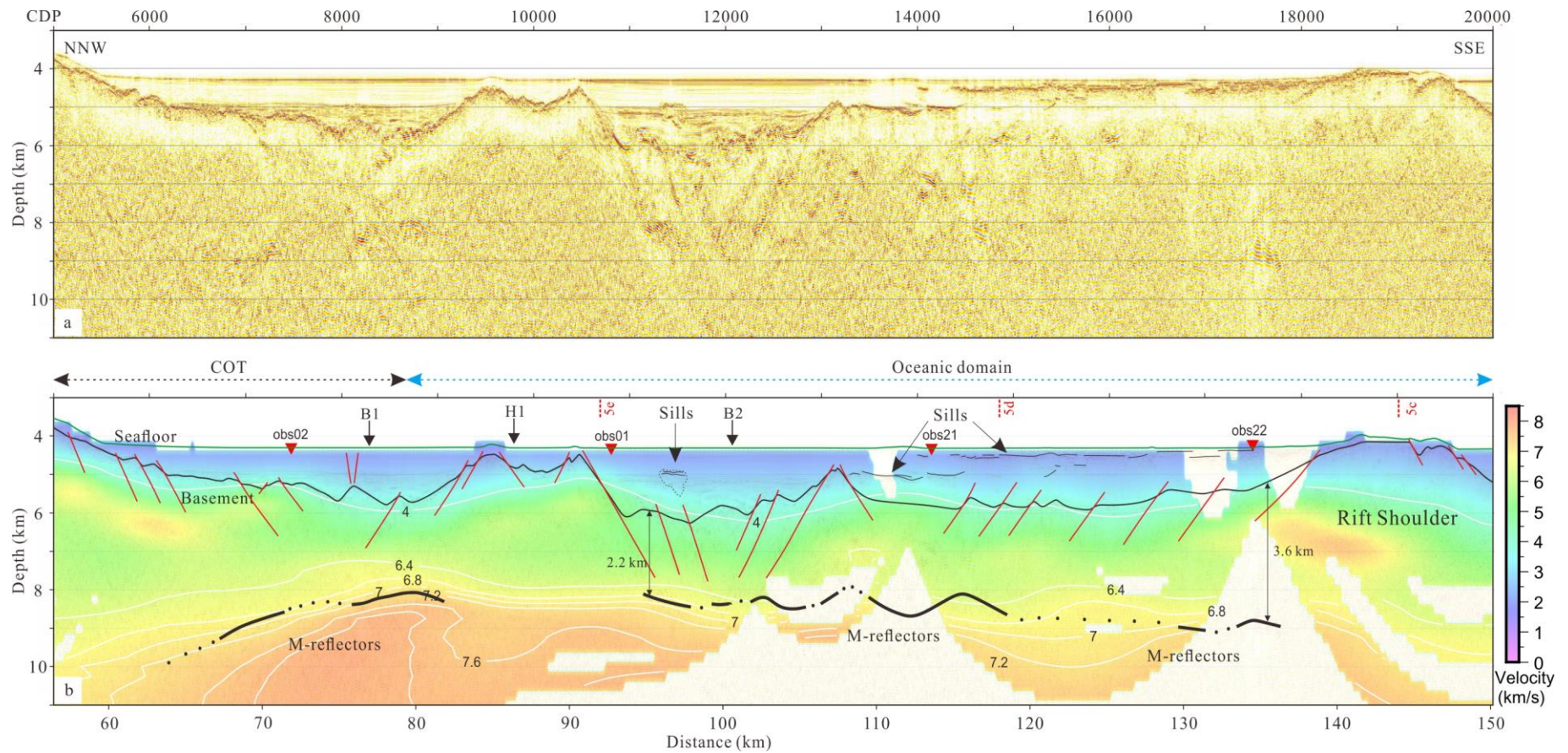
Fig.6. The uninterpreted (a) and interpreted (b) MCS section of profile NH973-1. See Fig.5a for location. Letters (B1-B2, H1) indicated with arrows in (b) designate specific features discussed in the text. The magnetic anomalies interpreted by Briais et al, 1993 are shown in red dashed lines (b). The red lines in (b) indicate normal faults. The corresponding velocity section from Fig.10d is projected in (b). Vertical exaggeration is 2.5.
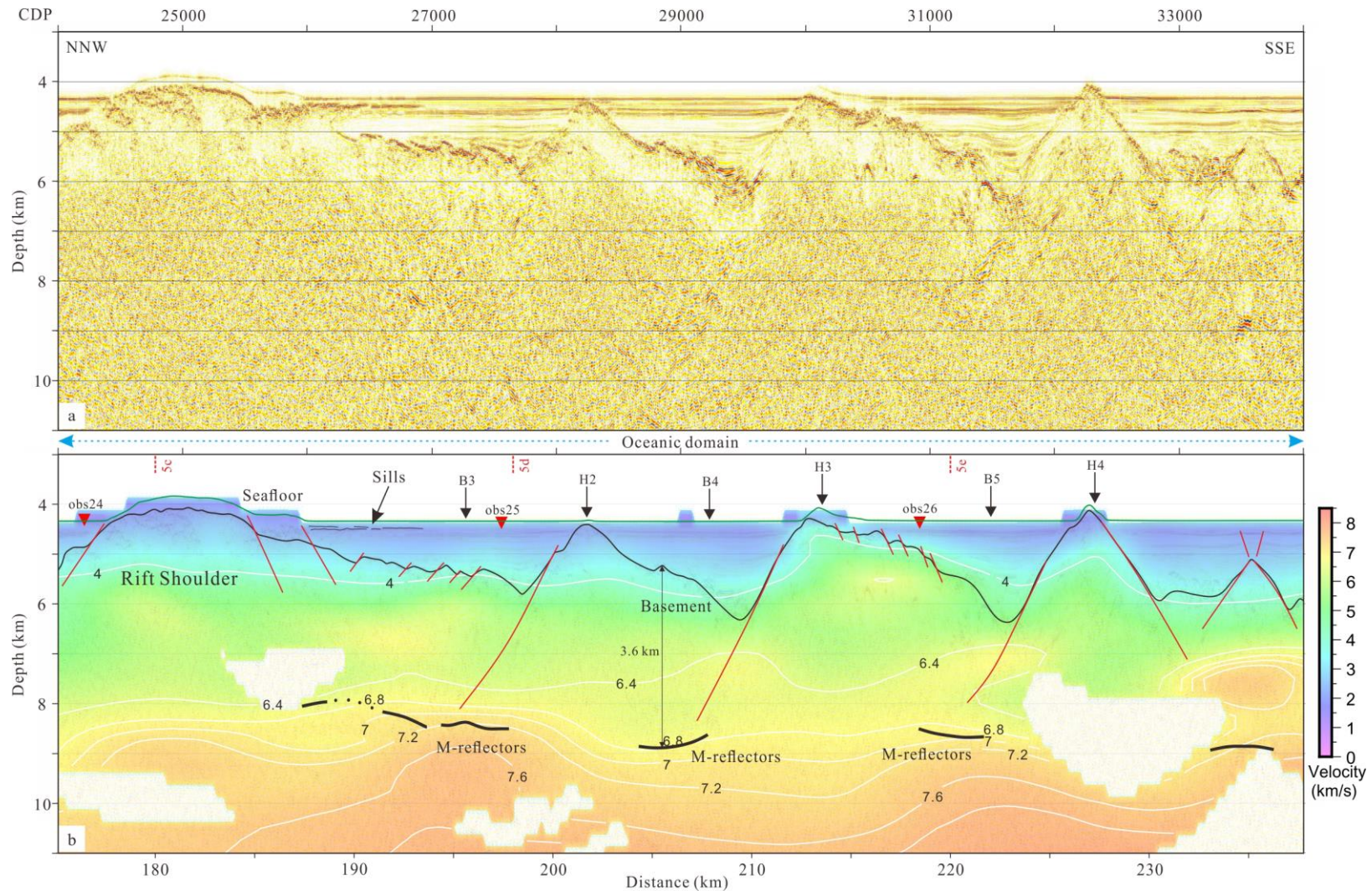
Fig.7. The uninterpreted (a) and interpreted (b) MCS section of profile NH973-1. See Fig.5a for location. Letters (B3-B5, H2-H4) indicated with arrows in (b) designate specific features discussed in the text. The magnetic anomalies interpreted by Briais et al, 1993 are shown in red dashed lines (b). The red lines in (b) indicate normal faults. The corresponding velocity section from Fig.10d is projected in (b). Vertical exaggeration is 2.5.
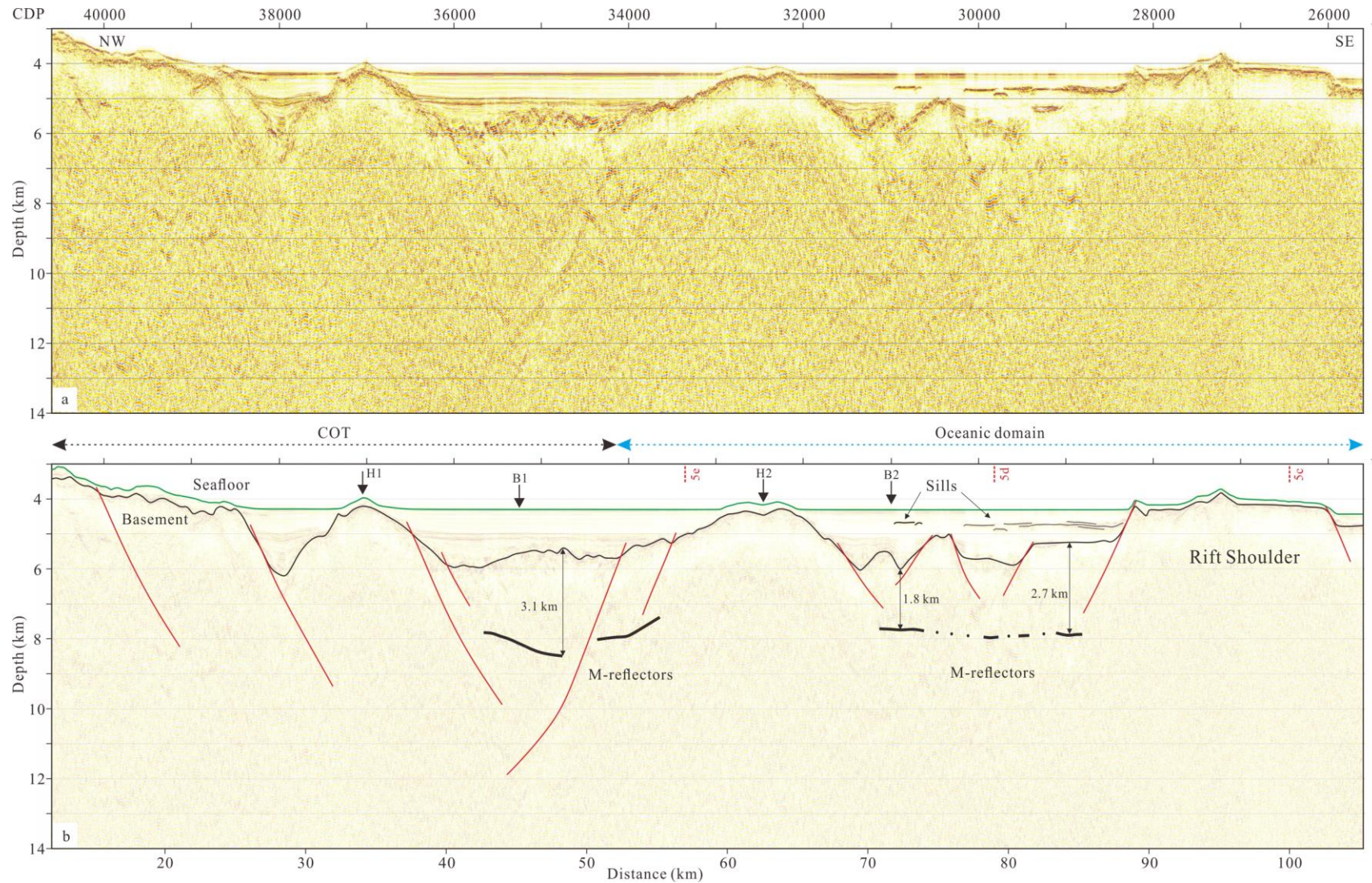
Fig.8. The uninterpreted (a) and interpreted (b) MCS section of profile CFCST-MCS2013. See Fig.5b for location. Letters (B1-B2, H1-H2) indicated with arrows in (b) designate specific features discussed in the text. The magnetic anomalies interpreted by Briais et al, 1993 are shown in red dashed lines (b). The red lines in (b) indicate normal faults. Vertical exaggeration is 2.5.

697
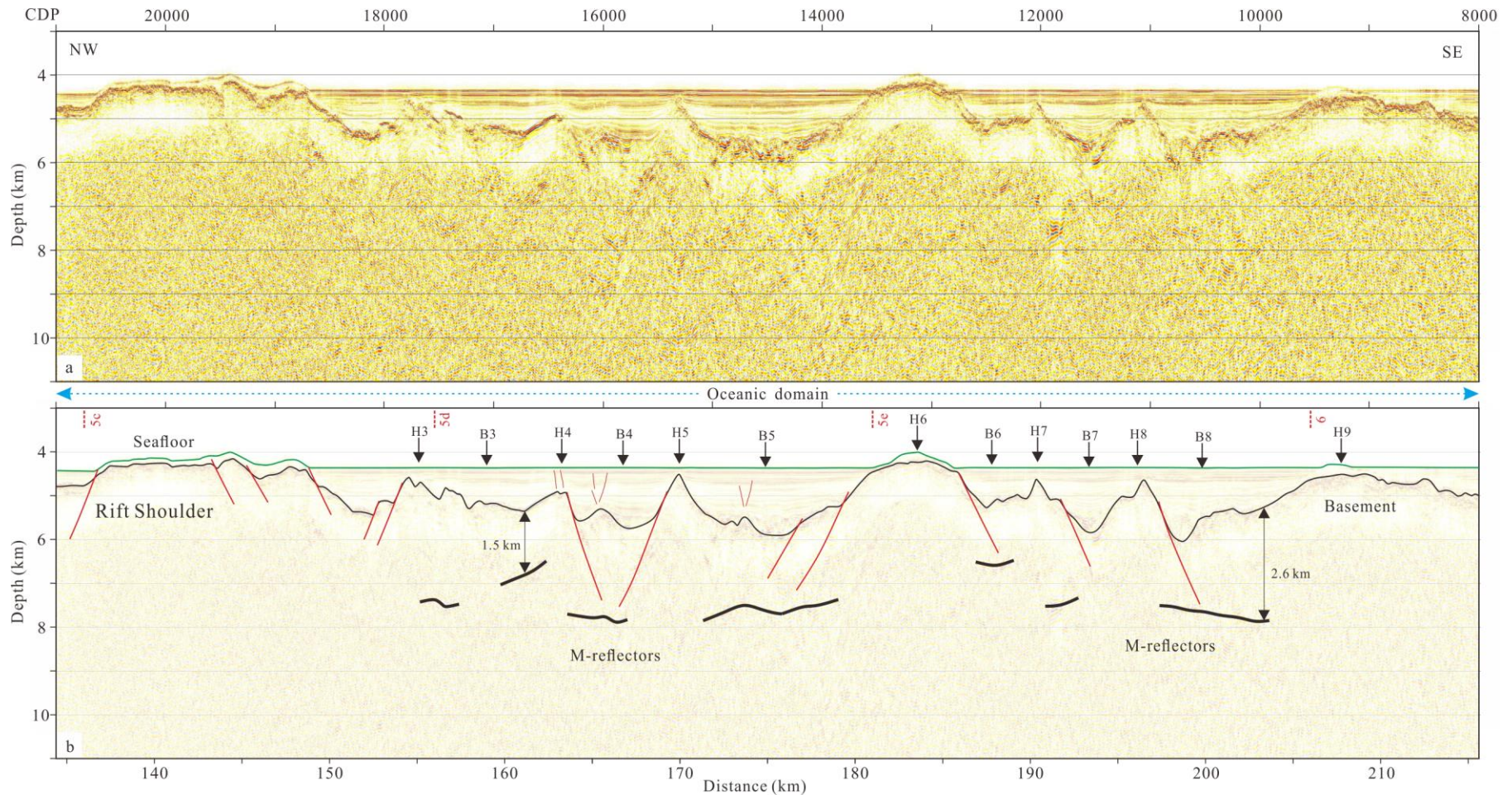
Fig.9. The uninterpreted (a) and interpreted (b) MCS section of profile CFCST-MCS2013. See Fig.5b for location. Letters (B3-B8, H3-H9) indicated with arrows in (b) designate specific features discussed in the text. The magnetic anomalies interpreted by Briais et al, 1993 are shown in red dashed lines (b). The red lines in (b) indicate normal faults. Vertical exaggeration is 2.5.

701
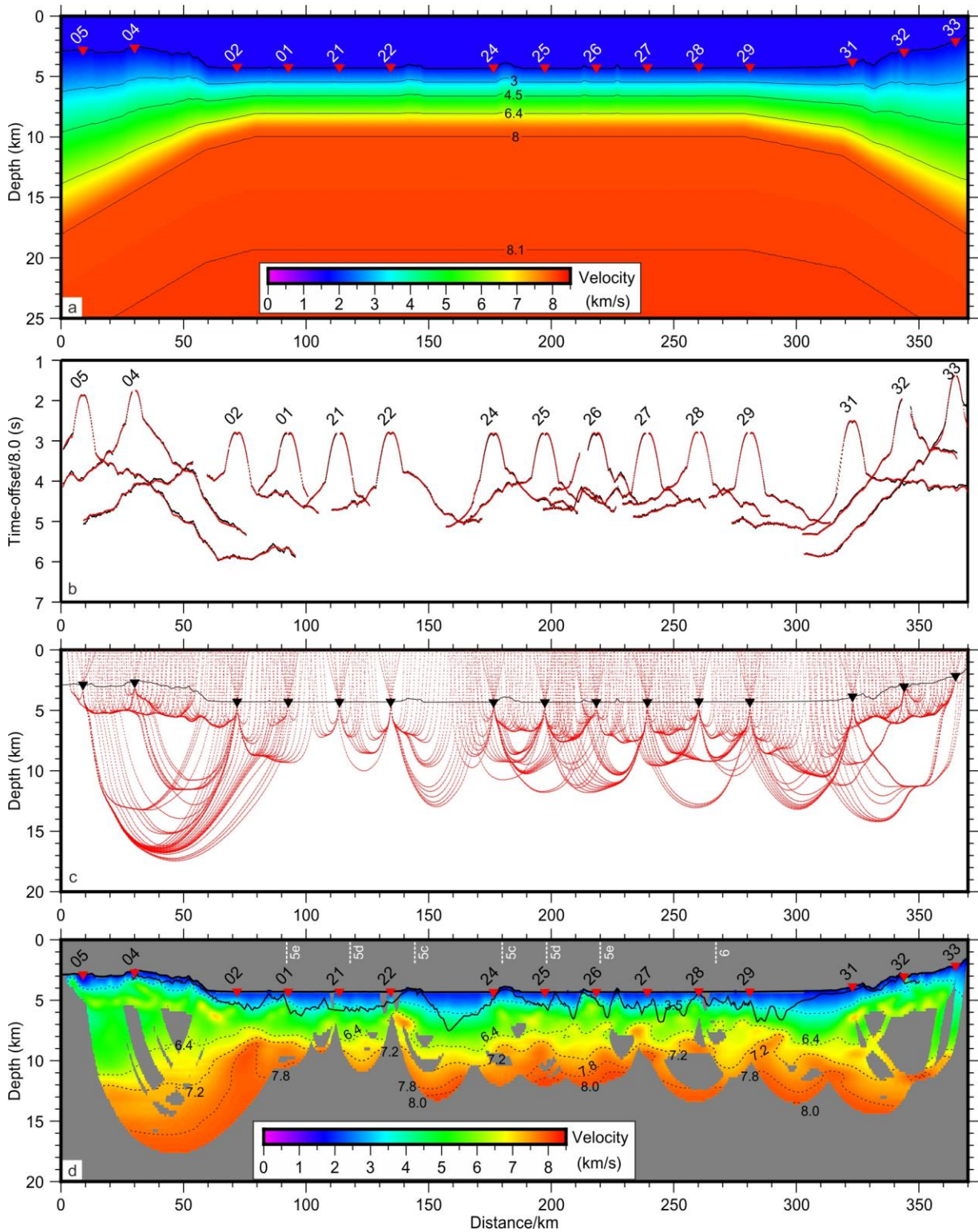
Fig.10. The initial velocity model (a), travel-time fitting (b), ray path (c) and final velocity model (d) of line OBS973. The black and red dots in (b) represent the picked and modeled travel time, respectively. Only one out of ten rays is shown in (c). The masked areas in (d) are not constrained by rays. The magnetic anomalies interpreted by Briais et al, 1993 are shown in white dashed lines (d).
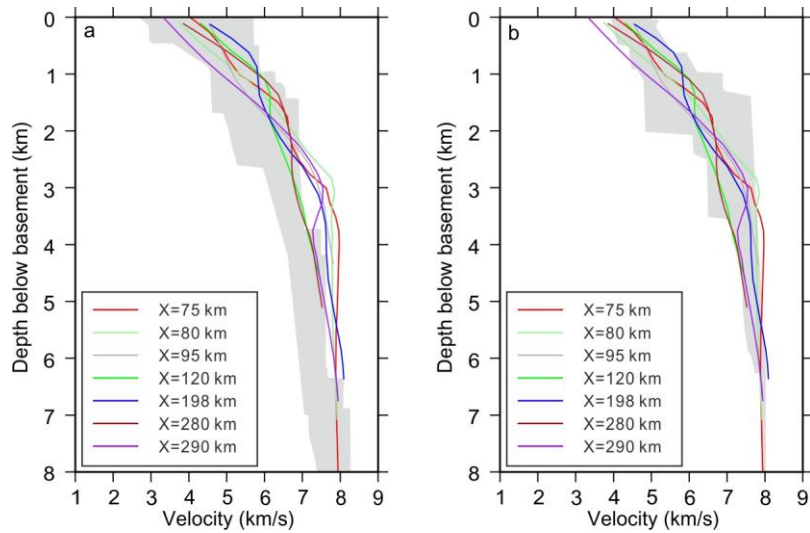
708

709 **Fig.11.** The 1-D velocity profiles through the final velocity model of OBS973 (Fig.9d). (a) The 1-D

710 velocity profiles compared to the velocity envelope for Atlantic oceanic crust aged 0-127 Ma (White

711 et al, 1992). (b) The 1-D velocity profiles compared to the velocity envelope for thin oceanic crust

712 overlying serpentinized mantle from Whitmarsh et al, 1996; Funck et al, 2003 and Davy et al, 2016.

713
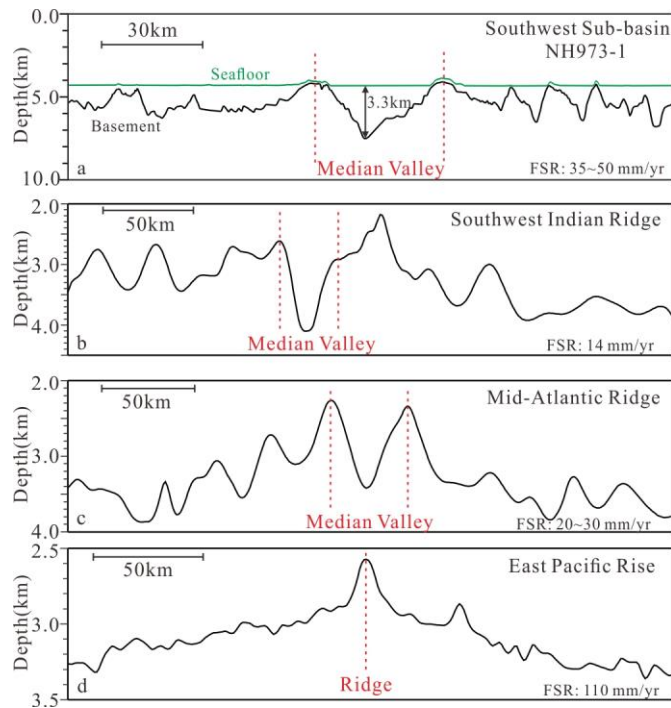
714

715 **Fig.12.** A comparison of morphologic profiles of the Southwest Sub-basin (a), the Southwest Indian

716 Ridge at 15°30'E (b), the Mid-Atlantic Ridge at 14°30'N (c), and the East Pacific Rise at 9°45'N (d).

717 Note the different scales. The values of full spreading rate (FSR) of the Southwest Sub-basin, the

718 Southwest Indian Ridge, the Mid-Atlantic Ridge, and the East Pacific Rise are from Li et al, 2014,

719 Dick et al, 2003, Grindlay et al, 1998, and Aghaei et al, 2014, respectively.

720 **Table 1**

721 Acquisition parameters of the MCS lines used in this study

Line	NH973-1	CFCST-MCS2013
Streamer channel	480	480
Channel interval (m)	12.5	12.5
Shot interval (m)	37.5	50
Record length (s)	12	16
Sampling rate (ms)	2	2
Minimum offset (m)	250	130
Air-gun volume (L)	83.3	83.3

722